SANDIA REPORT

SAND2018-10763
Unlimited Release
Printed Sept 2018

Conversion of Plastic Work to Heat: A full-field study of thermomechanical coupling

Amanda Jones, Elizabeth Jones, Ben Reedlunn, Sharlotte Kramer

Prepared by
Sandia National Laboratories
Albuquerque, New Mexico 87185 and Livermore, California 94550

Sandia National Laboratories is a multimission laboratory managed and operated by National Technology & Engineering Solutions of Sandia, LLC, a wholly owned subsidiary of Honeywell International Inc., for the U.S. Department of Energy's National Nuclear Security Administration under contract DE-NA0003525.

Sandia National Laboratories

Issued by Sandia National Laboratories, operated for the United States Department of Energy by Sandia Corporation.

Available to DOE and DOE contractors from
U.S. Department of Energy
Office of Scientific and Technical Information
P.O. Box 62
Oak Ridge, TN 37831

Telephone: (865) 576-8401
Facsimile: (865) 576-5728
E-Mail: reports@adonis.osti.gov
Online ordering: http://www.osti.gov/bridge

Available to the public from
U.S. Department of Commerce
National Technical Information Service
5285 Port Royal Rd
Springfield, VA 22161

Telephone: (800) 553-6847
Facsimile: (703) 605-6900
E-Mail: orders@ntis.fedworld.gov
Online ordering: http://www.ntis.gov/help/ordermethods.asp?loc=7-4-0#online

SAND2018-10763
Unlimited Release
Printed Sept 2018

Conversion of Plastic Work to Heat: A full-field study of thermomechanical coupling

Amanda R. Jones
Org. 1528, MS 0557
Sandia National Laboratories
P.O. Box 5800
Albuquerque, NM 87185-9999
ajones1@sandia.gov

Abstract

This project targeted a full-field understanding of the conversion of plastic work into heat using advanced diagnostics (digital image correlation, DIC, combined with infrared, IR, imaging). This understanding will act as a catalyst for reformulating the prevalent simplistic model, which will ultimately transform Sandia's ability to design for and predict thermomechanical behavior, impacting national security applications including nuclear weapon assessments of accident scenarios. Tensile 304L stainless steel dogbones are pulled in tension at quasi-static rates until failure and full-field deformation and temperature data are captured, while accounting for thermal losses. The IR temperature fields are mapped onto the DIC coordinate system (Lagrangian formulation). The resultant fields are used to calculate the Taylor-Quinney coefficient, β, at two strain rates rates (0.002 s^{-1} and 0.08 s^{-1}) and two temperatures (room temperature, RT, and 250^{o}C).

Acknowledgment

The authors would like to thank John Laing for his ingenious suggestions and knowledge of the equipment and Jay Carroll for the use of their lab space, including a brand new oven, which was instrumental in conducting this study.

Contents

List of Figures

List of Tables

Chapter 1

Introduction

Preventing material failure, especially under abnormal thermomechanical environments, requires understanding the underlying physics of material deformation. In ductile metals, plastic hardening during deformation can be strongly influenced by the local temperature and strain rates. Furthermore, large deformation (e.g. necking/ failure) can lead to substantial increases in temperature due to self-heating and localization. Unfortunately, the ability of models to accurately capture coupled thermal and strain rate effects in ductile metals remains highly limited by underlying assumptions regarding conversion of plastic work into heat generation (the Taylor-Quinney coefficient, β). Specifically, many thermomechanical models incorporate a constant value for β (ca. 0.9) independent of strain rate effects –an assumption that has been proven weak or invalid in the literature –and leads to large variations in model predictions. These assumptions have yet to be rigorously studied due to experimental limitations in delivering careful accounting of the thermal field under varying deformation rates.

In this study, we will utilize an emerging technique, combined infrared (IR) thermography with digital image correlation (DIC), to deliver simultaneous full-field measurements of temperature and deformation in response to quasi-static strain rates and moderate thermal environments. We have selected the mission- relevant material, 304L stainless steel, for this initial demonstration since the strain and temperature signals of 304L are well outside of the noise-floor of the aforementioned imaging techniques. DIC and IR thermography are currently at the forefront of material testing, but have not been leveraged in combination to understand the coupling of thermal environments, self-heating under deformation, and strain rate. This work seeks to demonstrate the ability of this method to lay the groundwork for a complete understanding of these coupled effects.

The final stage of the proposed research is to apply our measurements to preliminary calculations of β. To accomplish this research goal, we will need to account for the rate of heat loss terms (e.g. conduction, convection, and radiation) to the environment. Initial attempts will be made with textbook values but will be validated by heat transfer experiments (no mechanical deformation). While our focus is primarily on development of the experimental method, we will also show calculations for heat loss during a quasi-static test in order to have confidence that all measurements required are being considered. We envision that the validation of this technique will be a critical step towards a multi-material combined experimental and simulation effort, and accurate predictions of deformation and failure in abnormal thermomechanical environments.

Chapter 2

Experimental Method

In this section, the experimental design and implementation are described. As a precursor to the end goal of calculating β, a carefully controlled tensile experiment with simultaneous digital image correlation (DIC) and infrared (IR) thermography was conducted. Specimen geometry, experimental setup and baseline noise assessment/measurements will be discucssed.

2.1 Specimen Design

All specimens tested in the present work were 304L stainless steel (SS) dogbones with the same shape and dimensions shown in Figure 2.1, cut perpendicular to the rolling direction of the 304L sheet. These specimens were manufactured for a previous study, but were left untested. They fufilled many of the design requirements and as such were used for this work. A list of the requirements that we wished for in the present work are given below.

- Small Biot number, lumped capacitance assumption is valid: accomplished by having a thin specimen
- Long gage length in order to minimize conduction effects
- Small width to minimize surface area and heat loss (especially important as the length of the specimen increases)
- Reasonable dimensions for DIC/IR camera resolution
- Circular in order to give a true 1-D solution (only design requirement not accomplished by using this specimen geometry)

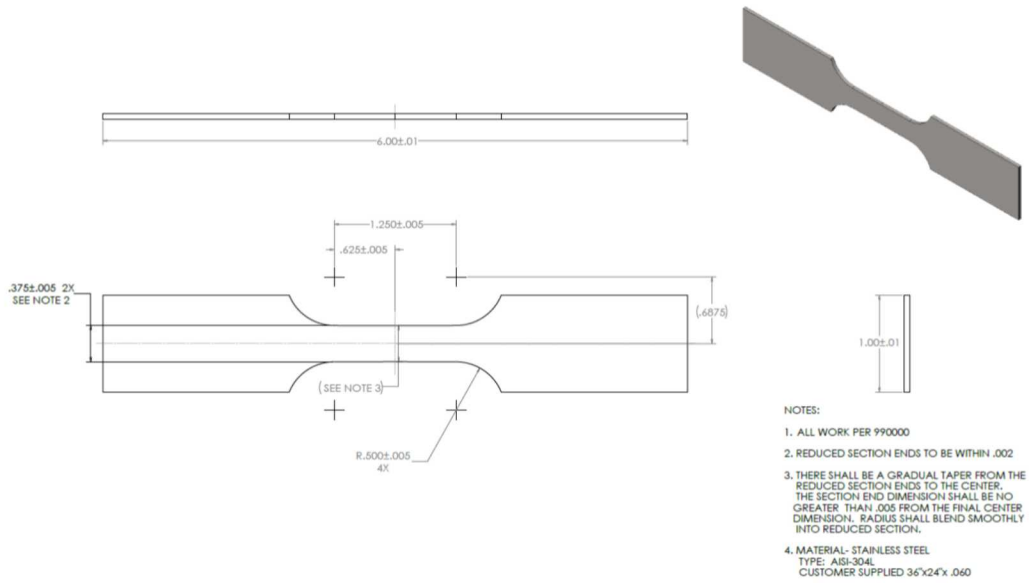

Figure 2.1: Tensile dogbone specimen geometry. Note all units are in inches.

2.2 Experimental Setup

Tensile testing was completed on a 330 kN load frame (MTS 311.21) in 701 (Material Mechanics Lab). The load frame was configured with an MTS actuator (Model: 204.32), calibrated within an 100 mm range, and an 180 kN load cell (Tovey, Model: SWP-22-40K-B000). High temperature mechanical grips (ADMET, part number: 3218-00443) were installed to threaded posts encircled by a stainless steel pipe with thermal grease at junctions to ease removal. The mounting scheme was designed to minimize heat transfer up the load train to the load cell/ actuator. A custom environmental chamber (Applied Testing Systems) was mounted to the load frame and the specimen was gripped inside (Figure 2.2). All specimens were precycled in load control to (20 N/s, amplitude: 444 N) in order to settle the specimen in the grips and then pulled to failure in displacement control at a prescribed displacement rate (between 0.0635 mm/sec and 2.54 mm/sec) and oven set point (between room temperature to 250^{o}C). For specimens tested at 250^{o}C, the sample was gripped in load control and allowed to freely expand (commanded to zero load) until thermal equilibrium was reached (ca. 2 h warmup time). This temperature, 250^{o}C, was the maximum possible to mostly eliminate paint debonding/cracking issues. Also, the oven was returned to room temperature before the next test to ensure consistent sample gripping conditions.

A plate/ custom viewport was designed (Figure 2.3) to hold 2 optical-grade glass windows (Edmund Optics, Part Number: 34-600, 50 mm diameter, 2 mm thick), an infrared window (Edmund Optics, Part Number: 68-818, 32 mm diameter, 3 mm thick), and a large window to increase the light that could get into the chamber (Technical Glass Products, 3.175 mm thick, polished 127 mm x 127 mm). The original experimental concept included a dichroic filtering mirror [1] and 2 large glass panes (one for DIC and one for IR), but concerns with shaking calibrated cameras (during opening and closing the chamber) and the expense of a single window for both optical and IR wavelength transmission led to a 3 viewport design.

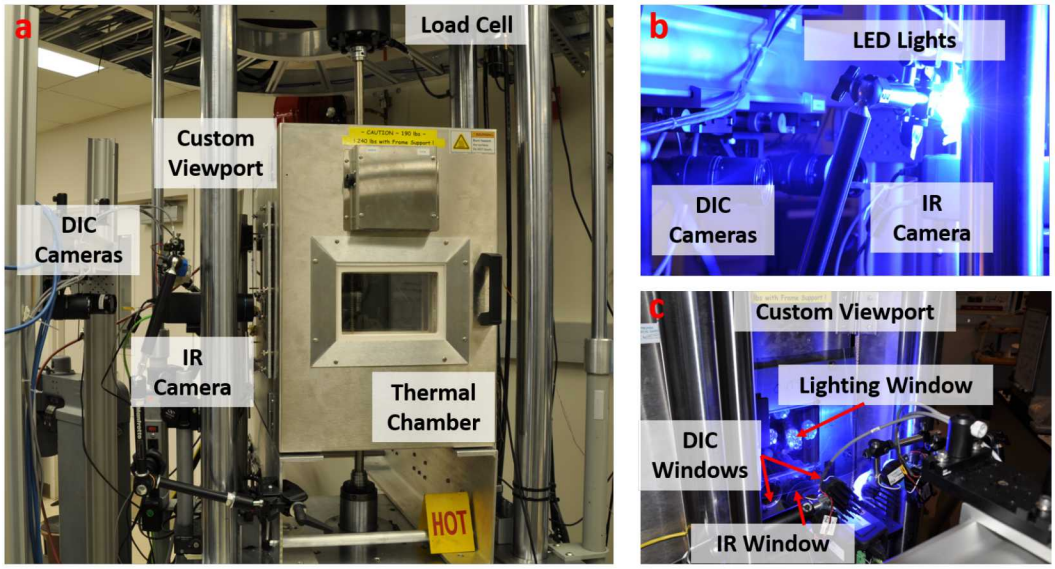

Figure 2.2: Experimental setup used in all tensile testing. (a) Global view of the whole setup showing the environmental chamber mounted in the load frame. (b) A zoomed in view of the DIC and IR cameras pointed towards the custom viewport and (c) side-view of the experimental chamber showing the individual viewport windows.

Prior to testing, all specimens were prepared for DIC/IR measurements. The specimen grips were masked and the specimen front was painted with white Rustoleum paint, which was selected for the relatively large displacements that can be achieved without paint cracking. Elevated temperature test specimens were additionally treated (before painting) with M-Prep Conditioner-A and M-Prep Neutralizer 5A as a mild etchant (followed by a neutralizer for the acid) to promote bonding of the paint to the surface. A white base coat (instead of individual particles of paint) was applied in order to keep a constant emissivity across the whole specimen. For room temperature testing, speckles were applied with a rolling stamp with black ink (Correlated Solutions). At elevated temperatures, this ink significantly degraded and so the black speckles were applied using an enlarged nozzle on a can of SEM black paint.

As mentioned above, a stereo-DIC system was used to monitor the displacements in and out of plane throughtout the duration of the test (left side in Figure 2.2). The DIC cameras used in this work were 2.5MP Grasshhopper USB3.0 cameras with Edmund Optics 75mm lenses and polalrizers mounted on the front of the lenses. Polarizers were oriented perpendicular to a polarizer placed in front of the lights to cross-polarize the light and eliminate spectral refractions from the Rustoleum paint. The working distance for this configuration was approximately 60 cm. The stereo angle between the cameras was approximately 21.5^o, with the specimen roughly centered between the two cameras. Furthermore, the cameras were oriented such that the long axis of the CCD chip was aligned (parallel) to the tensile pulling direction. The exact location in space of the cameras was measured using a commercial calibration routine, incorporated into Vic3D 8 software (developed by Correlated Solutions) and using a 3mm calibration target. Several advanced calibration routines have been developed by Correlated Solutions to aid with custom setups (such as setups with viewports/windows etc.), but the viewports and stereo angles used in this study did not war-

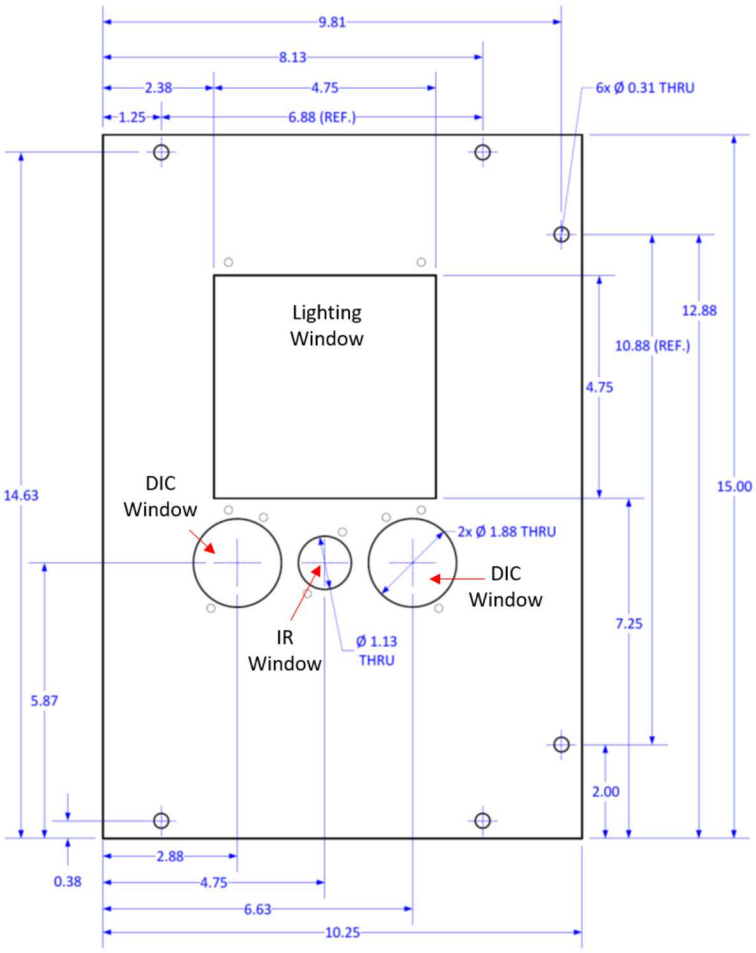

Figure 2.3: Plate designed to hold the windows with necessary properties to view the specimen.

rent use of these advanced routines (i.e. no significant change in noise was observed from using these advanced routines). Lastly, a low-velocity fan was placed in front of the cameras to keep the air in the optical path well-mixed.

For all specimens in this report, an identical set of DIC post-processing paremeters was used, which are shown in Table 2.1. All post-processing was conducted using a commercial software from Correlated Solutions, Inc. Virtual strain gauge studies were conducted on one specimen of each type to determine optimum post-processing parameters.

A noise floor (the error associated with DIC measurements) was defined as the standard deviation of the given parameter for a set of 5 static images and average values for all specimens tested are given in Table 2.2. Note that at elevated temperature, the noise floor is noticably higher than at room temperature. This is likely due to heat waves, which are difficult to remove from DIC measurements. Still, the noise floor is well below the 0.2% offset yield strain as well as the maximum strain observed for 304L (up to 0.7 engineering strain).

Table 2.1: DIC Post-processing Parameters

Post-processing Parameter	Setting
DIC Type	3D
Analysis Code	VIC-3D 8
Incremental Analysis?	None
Subset Weights	Gaussian
Correlation Interpolation Type	Optimized 8-tap
Correlation Criterion	ZNSSD
Subset Size (pixels)	25
Step Size (pixels)	3
Strain Type	Hencky
Strain Window	7

Table 2.2: Estimation of error in DIC measurements

Specimen Temperature	FOV	Noise Floor					
	(pix/mm)	U (mm)	V (mm)	W (mm)	$\varepsilon_{xx}(\mu\varepsilon)$	$\varepsilon_{yy}(\mu\varepsilon)$	$\varepsilon_{xy}(\mu\varepsilon)$
RT	20.92	0.0040	0.0009	0.0056	214	190	141
250^{o}C	20.92	0.0058	0.0053	0.0222	1275	1063	705

Though the noise floor was deemed acceptable for this application, numerical integration and derivatives of these experimental data was required and so a recursive low-pass filter (in time) was used to smooth the effects of heat waves. The parameters used were a cut-off frequency of 0.15 sec and an order of 1 (using the commercial routine developed by Correlated Solutions). For consistency, this filter was applied to all data.

Temperature measurements were taken using an IR camera and thermocouples. The IR camera used in this work was from FLIR (Model: A655sc, 640 x 480 pix, 50 fps, $\pm$ 2^{o}C) with a 13 mm focal length lens controlled using commerical ResearchIR software. Calibration/ customizing of the software parameters will be discussed in Section 2.4. The IR camera resolution (and lensing) was one of the main limiting factors in this work (compared to DIC measurements). Thus, the IR camera was placed as close to the custom viewport as possible (maximize magnification), while not risking undo heating of the camera. At this placement, distance from specimen equal to 0.2699 m, the FOV was approximately 2.94 pix/ mm.

Thermocouple data, at a number of locations, was acquired using an NI cDAQ 9188 system (thermcouple acquisition card: NI-9213, Analog Out card: NI:9264). Thermocouples were used to monitor the viewport temperature and the air temperature in between the IR camera and the side of the oven, as well as taped (with thermal paste in between) to the gage section, both sides of the grips and at several locations inside the chamber (including the chamber wall). Taping was, however, not particularly ideal, and the thermocouple measurements were used more as sanity checks than truth values. The exception to this statement was the few datapoints taken with a welded thermouple and the oven air temperatures (no tape involved) and the measurements taken outside the chamber (no deformation, true steady-state environment).

All of these measurements (DIC cameras, IR camera, thermocouples) were hardware synced by using a TTL pulse from the MTS FlexTest 40 controller. For this study, we used a pulse to start these 3 measurement schemes on the same initial pulse, but assume that the timestamp from the various control softwares is accurate after the initial pulse. A potentially more accurate method to sync would be to pulse trigger, but many of the customizable features of the various softwares are lost if you use this technique. Still, future work may benefit from looking into this further.

2.3 Heat Lost to Convection

One unique element of this work is that in addition to simultaneous thermal and deformation measurements, the heat lost to the environment also needed to be quantified. Traditionally, this type of analysis (determination of the ratio of plastic work converted to heat) is done on a Kolsky bar (high rate testing apparatus) so that an adiabatic assumption can be made (heat loss to convection, conduction, radiation neglected). Unfortunately, it is still difficult experimentally to do the type of high resolution measurements we desired (involving both high speed DIC and IR in a thermal soak condition/ environmental chamber) on a Kolsky bar setup. As a result, this work took a different approach but with the added difficulty of calculating the heat losses to the environment.

In order to measure the convectional heat losses we used a heat flux sensor (RdF Corp, Part Number: 27036-1) affixed to the specimen with thermal paste (Omega). The sensor appears much like a strain gage and operates under similar principles. There are small wires embedded in a polymer film that change resistance and output a signal in μV which is calibrated to a heat flux in W/m^2 based on the temperature of the sensor (a Type T thermocouple is also embedded in the sensor for this purpose). Thus, the apparent heat transfer coefficient, h_a, can be described by the equation:

$$h_a = \frac{EC\theta(T_s)}{(T_\infty - T_s)}, \tag{2.1}$$

where E is the heat flux output signal in μV, C is the calibration factor in $\mu V/W/m^2$, $\theta(T_s)$ is the correction to that calibration factor depending on the temperature of the specimen (T_s), and T_∞ is the far-field temperature of the environment. Since the heat flux sensor is measuring the total heat flux off the surface, h_a represents the combination of both radation and convection losses or:

$$h_a = h_r + h_c, \tag{2.2}$$

and the radiation contribution can be subtracted out using:

$$h_r = \varepsilon\sigma(T_s + T_\infty)((T_s^2 + T_\infty^2). \tag{2.3}$$

In this experiment, the specimen was unpainted and so the contribution to radiation was quite small (using textbook value for emissivity, ε of 304L SS= 0.05 and σ, the Stephan-Boltzman constant).

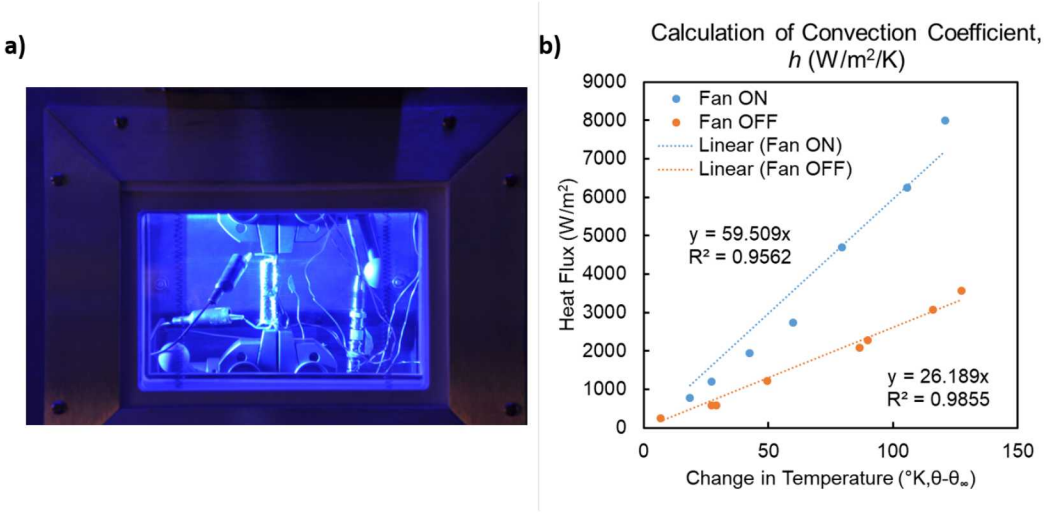

Figure 2.4: (a) Image of the resistive heater setup for convection characterization. (b) Calculation of the convective heat transfer coefficient for both the fan on and fan off.

We originally desired to use this sensor throughout mechancial testing, but it was too heavy to stay affixed with just the thermal paste, no matter what attachment mechanisms we tried. As a result, we ran a series of experiments where we input heat using a resistive heater into the specimen. The specimen was mounted in the grips and the grips were set to control to zero load (allow free thermal expansion). The chamber was controlled to room temperature with the fan on and off, and the air tempearture was monitored. The convective heat transfer coefficient ($h_c, W/m^2/K$) can then be calculated directly. Unfortunatley, the sensor's max temperature was near 250^{o}C and using the resistive heater at temperature was suspect, so the series could only be conducted with the far-field temperature equal to room temperature.

2.4 IR Camera Calibration

First, the IR camera factory calibration was checked against a blackbody source (cavity type). ResearchIR software allows you to change "Object Parameters" based on your situation (see screenshot of parameters used here in Figure 2.5). For the factory calibration check, the blackbody source was placed at the same distance away from the IR camera as the specimen in the real test, with the IR window at approximately the same relative position in between the blackbody source and the camera. The IR camera lens was then focused and the object parameters were set to a distance = 0.2699 m, emissivity = 0.98 (typical for blackbody source), and lens transmission to 0.9 (per the manufacturer's specification). All temperatures were left at 23^{o}C as a typical room temperature for the lab and humidty was left at 50% per instructions from Ross Overstreet (FLIR Technical Support Representative).

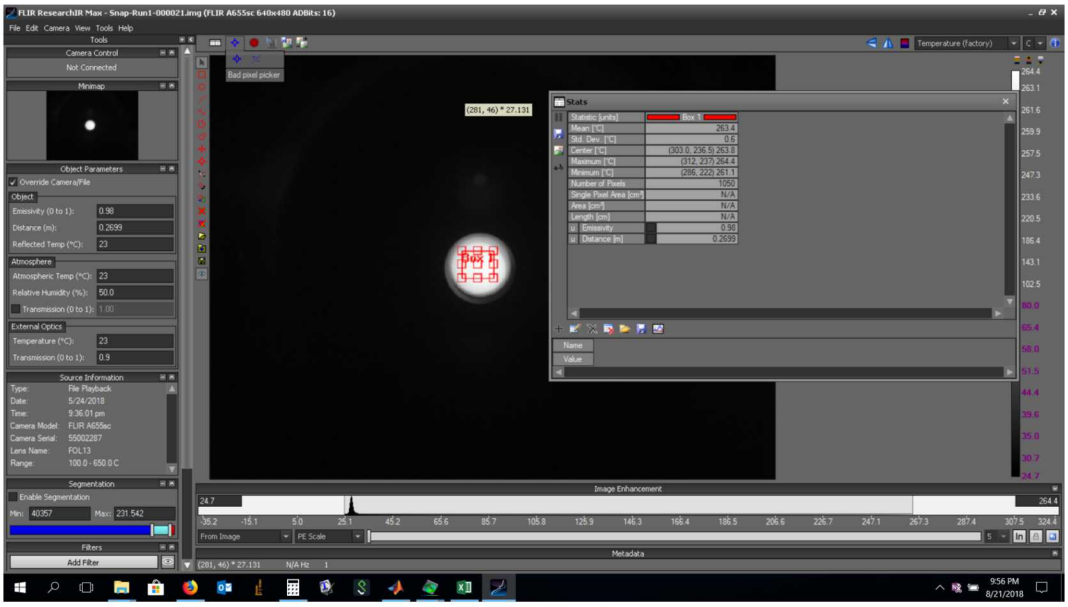

Figure 2.5: Screenshot of the ResearchIR software interface, an image of the blackbody source and the object parameters used.

The temperature of the blackbody source was swept up to the maximum temperature observed in the course of the experiments. Note, the lens has 2 factory calibration settings: 1) from -40^{o}C to 150^{o}C and 2) from 100^{o}C to 650^{o}C. The appropriate range was selected for the temperature of the blackbody source and the results are shown in Figure 2.6a. At all temperatures the % Difference was within the manufacturer's specification for the accuracy of this IR camera ($\pm$ 2^{o}C or 2% of reading).

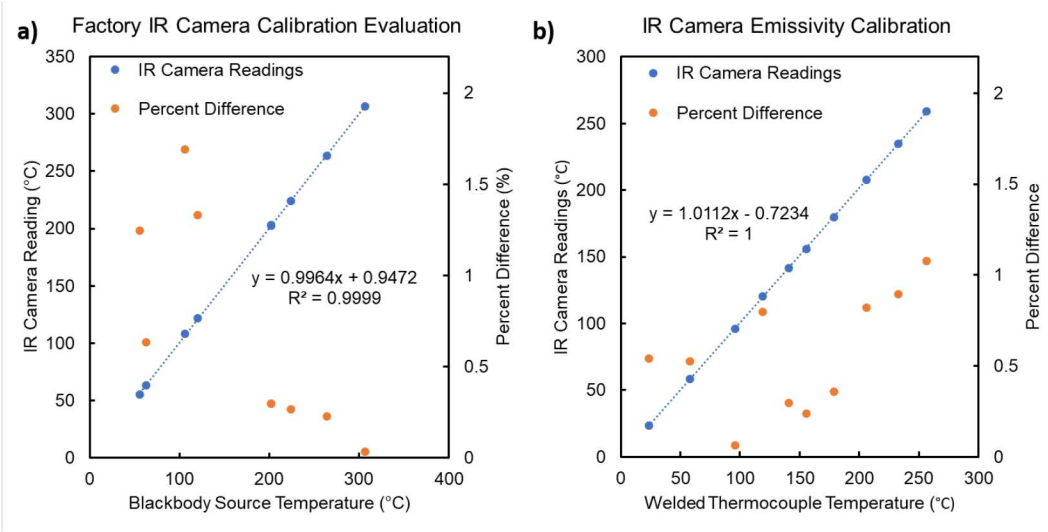

Figure 2.6: IR camera calibration. (a) Blackbody IR camera calibration showing less than 2% difference (manufacturer's specification) in all cases. (b) Emissivity and reflected temperature calibration showing less than 1% difference from welded thermocouple measurements.

Second, the emissivity and reflected temperature were calibrated per the instructions from Ross Overstreet. The reflected temperature changed as the oven temperature changed, and was calibrated using a piece of crumpled foil tape with emissivity set to 1. The foil tape temperature at each snapshot taken was set to the reflected temperature value. Then the emissivity calculator was used to set the temperature of the paint equal to a piece of electric tape temperature (emissivity=0.96). The average value of 0.89 for the paint was obtained and the error in the measurements using that emissivity and a reflected temperature that was fit to the oven set point is shown in Figure 2.6b. Again, error was less than 2% of the accepted value (in this case the welded thermocouple), but it is worth noting that these conditions represent an undeformed specimen and do not take into account error from paint changing emissivity and/or cracking during testing.

Chapter 3

Results

In this section, the results of the tensile tests run will be compared and the calculation of β methodology will be outlined. The ability to quantify β as a function of temperature and strain rate will also be discussed.

3.1 Global Response

First, the engineering stress-strain results are shown in order to quickly determine if the results are similar to prior published data (Figure 3.1). The material used here is the same used in SAND2015-9012, written by Kramer et al. [2] and the tabulated results are in good agreement with those tensile tests (Table 3.1). Table 3.1 also includes the maximum temperature observed at the end of each tensile test. The change in temperature was noticably different for testing case (rate and temperature), but the stress-strain curves were only noticably different for the room temeprature tests. At the elevated temperature, the stress-strain curves were almost indistinguishable, suggesting that temperature effects dominated over strain rate effects.

Table 3.1: 304L Test Results Summary.

Specimen	Displacement Rate (mm/sec)	Nominal Eng. Strain Rate (ε/sec)	Oven Temperature (^oC)	Peak Stress (MPa)	Strain at Peak (mm/mm)	Strain at Failure (mm/mm)	Max. Temperature (^{o}C)
Beta-S8	0.0635	0.002	*RT*	788.5	0.57	0.67	76.2
Beta-S9	0.0635	0.002	*RT*	786.6	0.57	0.69	69.7
Beta-S12	0.0635	0.002	*RT*	789.7	0.55	0.67	64.8
Beta-s10	2.54	0.08	*RT*	781.4	0.38	0.49	>150
Beta-S24	2.54	0.08	*RT*	786.3	0.40	0.50	>150
Beta-S16	0.0635	0.002	250	475.3	0.31	0.39	259.2
Beta-S20	0.0635	0.002	250	470.1	0.31	0.40	266.3
Beta-S18	2.54	0.08	250	472.2	0.31	0.39	303.8
Beta-S22	2.54	0.08	250	477.6	0.31	0.38	294.5

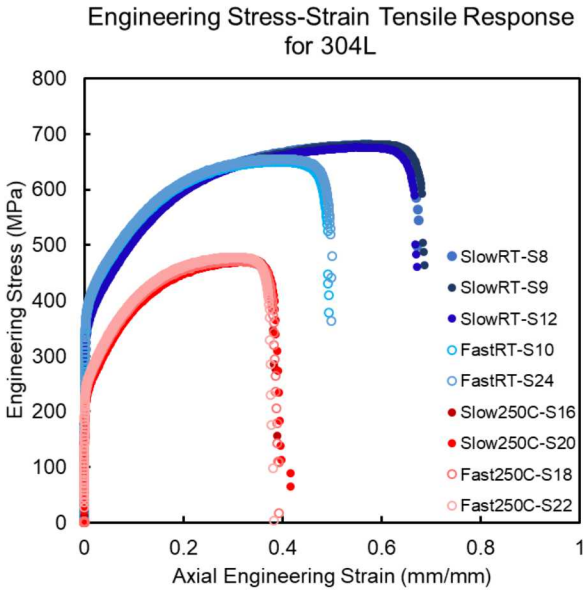

Figure 3.1: Engineering stress-strain response for the 4 conditions (slow rate, 0.002 s^-1 and RT, fast rate, 0.08 s^-1 and RT, slow rate, 0.002 s^-1 and 250^{o}C, fast rate, 0.08 s^-1 and 250^{o}C) tested in this work.

3.2 Evaluation of the Taylor-Quinney Coefficient β

The 1-D description of thermomechanical deformation has been derived in the literature [3] and is described (in Lagrangian coordinates) as:

$$\rho c\theta_t - k\theta_{xx} = Q_t^p + Q_t^e + r. \tag{3.1}$$

In Equation 3.1, ρc is the heat capacity in $J/m^3/K$, k is the thermal conductivity in $W/m/K$, Q_t^e is the elastic heating which is generally neglible, r is internal power supply (here, r=0), and the plastic heat generated, Q_t^p, is described by:

$$Q_t^p = \beta W_t^p - \frac{A_s}{V}[h(\theta - \theta_\infty) + \hat{\sigma}\tilde{\varepsilon}(\theta^4 - \theta_\infty^4)]. \tag{3.2}$$

In Equation 3.2, the fraction of plastic work converted to heat (βW_t^p) is calculated and the energy lost to the environment (through convection and radiation) is subracted, where h is the convective heat transfer coefficient, A_s is the surface area of the specimen, V is the volume of the specimen, θ is the temperature of the sample, θ_∞ is the far-field environment temperature. Radiation loss is described using $\hat{\sigma}$ is the Stephan-Boltzman constant, and $\tilde{\varepsilon}$ is the emissivity of the specimen multipled by the temperature difference between the sample surface and far-field temperature. The heat lost to conduction is accounted for directly though the $k\theta_{xx}$ term in Equation 3.1. For the

present study, the thermal conductivity, k, and the heat capacity, ρc, constants are obtained as a function of temperature from from Assael and Gialou [4]. Thus, β can be calculated by:

$$\beta = \frac{1}{W_t^p}[\rho c\theta_t - k\theta_{xx} + \frac{A_s}{V}[h(\theta - \theta_\infty) + \hat{\sigma}\tilde{\varepsilon}(\theta^4 - \theta_\infty^4)]]. \tag{3.3}$$

Historically, the determination of β has been accomplished on a Kolsky bar so that all heat loss terms can be neglected (adiabatic conditions) [5] . In the present study, we will evaluate the robustness of a quasi-static analysis, which can more easily utilize full-field techniques (DIC/IR). It is worth noting at this point several key assumptions/ limitations.

- DIC and IR thermography measure surface displacements and temperatures respectively and the equation above is in units of Watts/Volume. Therefore, the key assumption is that the strains/ temperatures are valid through the thickness, which is accomplished by using a thin specimen.

- Only 1-D force measurements were taken (load cell above the specimen), and thus a 1-D analysis is used, which becomes invalid as soon as significant necking is observed. The strain/temperature data is collapsed to 1-D by averaging across the width of the specimen.

The first step, then, in conducting such an analysis, is to map the IR data onto the DIC data (Lagrangian coordinates). A suite of scripts was developed by Elizabeth Jones to accomplish this task. A list of the main functions of these scripts are given below.

- Sync the two coordinate systems: 1) from the DIC analysis and 2) from the IR camera.

- Map the IR data onto the DIC displacement nodes (interpolation necessary due to the lower resolution of the IR camera).

- Average the axial true strain across the width. Here, we only have a 1-D stress state and to do a 2-D description of β would require a model, which was outside the scope of this work.

- Calculate the true stress using DIC measurements and assuming isotropy for out of plane strain (i.e. $\varepsilon_{eng,yy}$=$\varepsilon_{eng,zz}$), where $\varepsilon_{eng,yy}$ and $\varepsilon_{eng,zz}$ represent the transverse engineering strain and through-thickness engineering strain respectively. Note, there are more rigorous methods to estimate true stress from DIC data (e.g. using plastic incompressibility), but the methods tried here did not noticably change the results and thus the isotropy assumption was deemed sufficient for this intial case study.

- Calculate the plastic work rate using the work conjugate pair of true stress and true plastic strain rate where

$$W_t^p = \sigma_{xx}\varepsilon_{t,xx}^p. \tag{3.4}$$

  Note: at this stage results were truncated at peak load to ensure a 1-D stress state was valid

(minimal necking).

- Calculate the temporal and spatial temperature derivatives.
- Combine the above results to calculate β as shown in Equation 3.3.

3.3 Case Study: RT, Fast Strain Rate

In this section, example curves used in the ultimate calculation of β will be outlined for the easiest case of a RT test at a relatively fast quasi-static rate (approaching adiabatic conditions). First the calculation of the plastic work rate is shown, which begins with calculation of the true stress and true plastic strain. In Figure 3.2a, the complete curve for true stress and true strain is shown as outlined in Section 3.2 with respect to three locations along the gage: (1) near the stationary grip, (2) at the center, labeled "gage," and (3) near the moving grip. These three locations collapse for the majority of the tensile test, until the strain starts to localize in the center of the gage. The plastic strain is calculated as:

$$\varepsilon_{xx}^{p} = \varepsilon_{xx,meas} - \varepsilon_{xx}^{e} = \varepsilon_{xx,meas} - \sigma/E, \tag{3.5}$$

which is shown in Figure 3.2b.

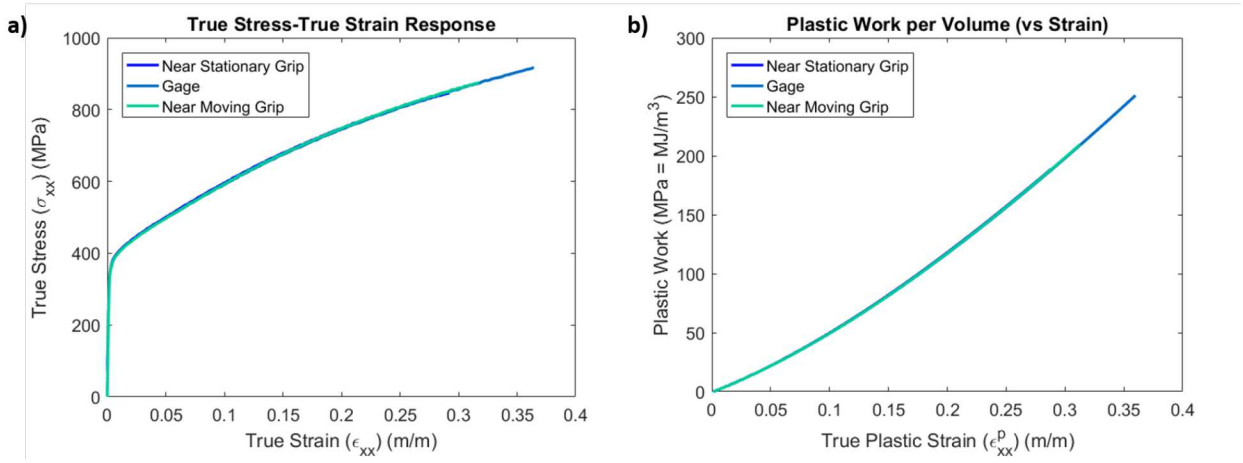

Figure 3.2: (a) True stress vs true strain as a funtion of location along the gage length for a specimen tested at the fast, 0.08 s^{-1}, strain rate at room temperature and (b) corresponding plastic work versus true plastic strain.

Then by combining terms as described in Equation 3.4, the plastic work rate is calculated and shown in Figure 3.3. Noise is inevitable when taking derivatives of experimental data and care was taken not to over-smooth any of the results. Fitting these curves will be discussed in the final section of this work.

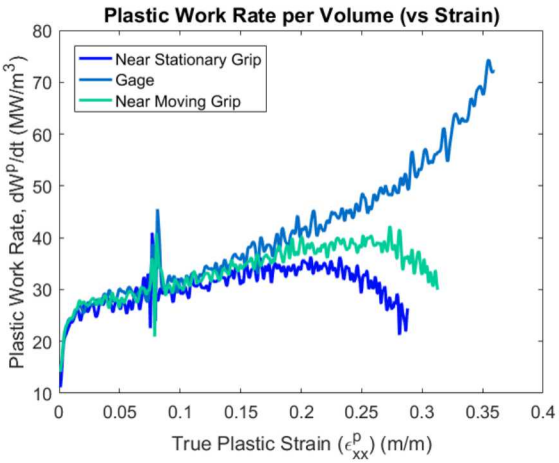

Figure 3.3: Plastic work rate as a funtion of location along the gage length for a specimen tested at the fast, 0.08 s^{-1}, strain rate at room temperature. Note, the jump at ca. ε^p= 0.07 is due to a glitch in the camera acquisition rate.

The temperature results form the second critical component of this analysis and are shown in Figure 3.4. Similar to the plastic work, the temperature gradually increases with strain, slightly more so in the gage section. Again, the temperature temporal derivative in Figure 3.4b is a source of noise that will be discussed later.

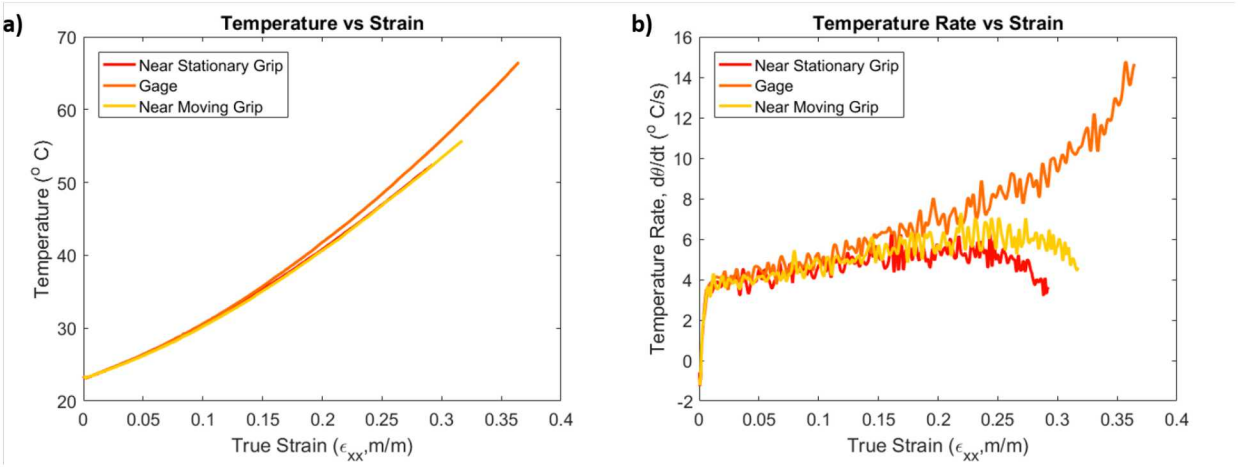

Figure 3.4: (a) Temperature vs true strain as a funtion of location along the gage length for a specimen tested at the fast/ 0.08 s^{-1} strain rate at room temperature and (b) temporal derivative of temperature versus plastic strain

Finally, the spatial derivative of temperature is required and Figure 3.5a shows the progression of the spatial temperature field with time. Several piecewise local linear fits were tried before going with a quadratic fit of the full length of the gage (Figure 3.5b). Though this assumption/ method could be improved upon, the spatial derivative of temperature is relatively small no matter the fitting parameters used and has only a small impact on the final results.

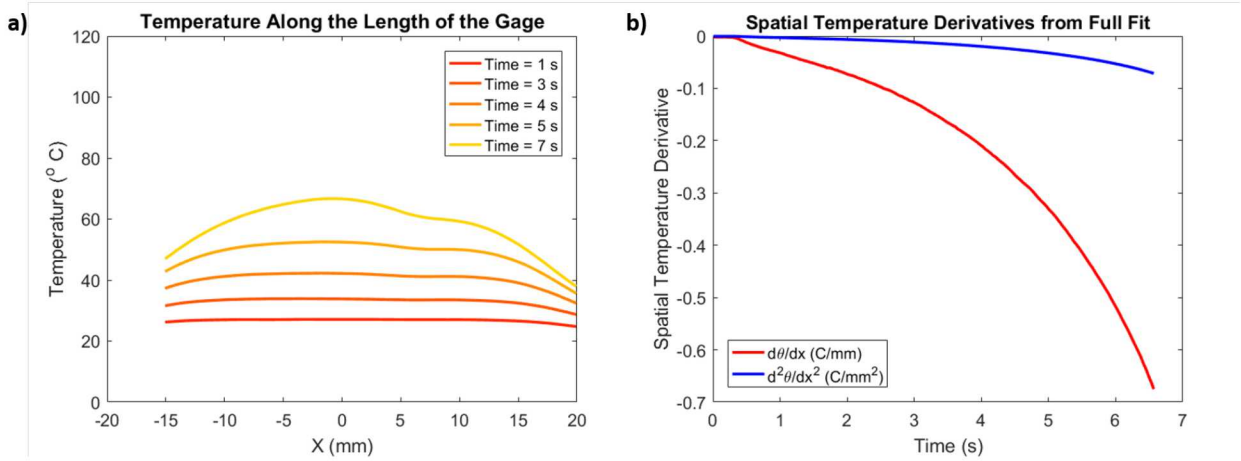

Figure 3.5: (a) Temperature vs location along the specimen as a funtion of test duration at the fast/ 0.08 s^{-1} strain rate at room temperature and (b) spatial derivatives for temperature acquired by fitting the entire specimen length with a quadratic curve.

Putting it all together, Figure 3.6a shows each of the individual terms that go into the calculation of β as per Equation 3.3. One important take-away is that the losses for this case (conduction, radiation, and convecction) are small compared to all of the other signals. In other words, full-field calculation of β should be possible at "fast" quasi-static rates. Figure 3.6b shows the relationship between β and the plastic strain for several locations along the specimen. When we began this work, the method had been attempted, with some differences, in a nice piece of research from Knysh and Korkolis [6]. Even so, they saw large fluctuations in their results for β, with about a span of 0.5 (half of β). Compared with these literature results, the noise here is much reduced. Some reasons for this could be (1) using the full-field results to calculate the second spatial temperature derivative, (2) operating in Lagrangian coordiates and eliminating one of the the derivative terms, (3) the use of stereo-DIC for true stress calculation and/or higher accuracy DIC results. Lastly, the other noticable feature, is that β does not equal 0.9, which is the commonly accepted value, nor is it constant with respect to plastic strain.

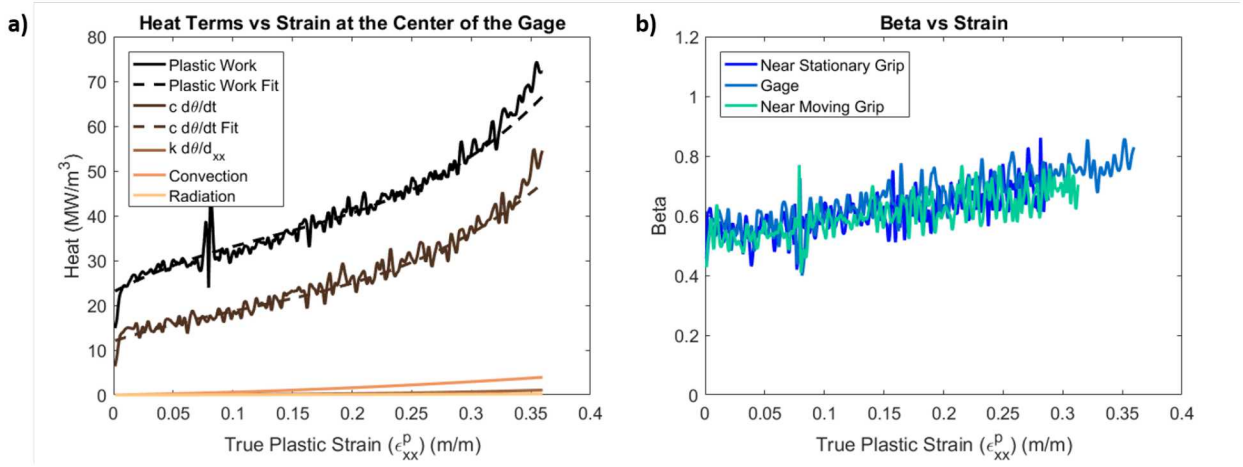

Figure 3.6: (a) Heat flux terms from each term in Equation 3.3 at the center of the gage and (b) calculation of β at three locations: near the stationary grip, at the center of the gage, and near the moving grip.

3.4 Effect of Strain Rate and Soak Temperature on β

With the groundwork laid in Section 3.3, the effects of strain rate and soak temperature were studied. These environments proved more challenging than the RT, fast case. Figure 3.7a shows the same heat flux terms quantified above, but the noise in the plastic work rate increased (likely due to heat waves from the DIC results) and the thermal signal-to-noise ratio decreased (lower ΔT) leading to more noise in the temperature rate calculation. Still, a similar gradual upward trend is observed, when compared to the fast, RT case, and the majority of the data in the center of the gage resides within ± 0.1 β.

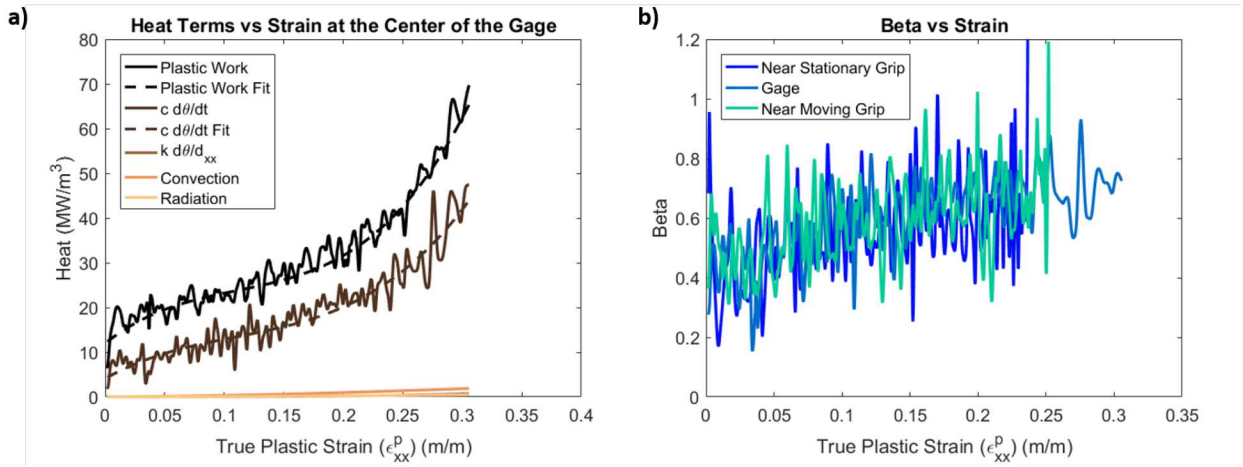

Figure 3.7: (a) Heat flux terms from each term in Equation 3.3 at the center of the gage and (b) calculation of β at the fast/ 0.08 s^{-1} strain rate and 250^{o}C.

The other main issue we observed was related to the convection measurements. The values for the

convective heat transfer coefficient were between textbook values, but the textbook calculations ranged anywhere from 0.75-2x the measured value of 59.51 $W/m^2/^oK$ (for the fan on). Additionally, the convection heat term was sensitive to the far-field temperature, which was at best a guess from point-wise thermocouple measurements. As a result, we assumed that the initial temperature of the specimen was the far-field temperature, as the specimen would have been in equilibrium before the test and the oven uniformity was in question. One improvement for future studies would be to use the IR camera to quantify the far-field temperature by placing an undeformed metal painted piece nearby.

Still, it may also not be possible to get an accurate convective heat loss measurement without a thermal model of the chamber. For the fast rates, the convection effects were so small compared to everything else that this was less of an issue. But, for the slow rate– even though we attempted to ballpark the slowest we could go using estimates of the expected results– the calculation can go into a range $\beta > 1$ which is not physically possible. As an alternative/ addition to a thermal model, we could also employ a vacuum tube as used in the work by Knysh and Korkolis [6]. We were hopeful that using a vacuum tube would prove unnecessary, especially since DIC through one chamber window into an oven is challenging to begin with, but this might be unavoidable. These observations are summarized in Figure 3.8, where the convection is noticably higher for the two slow cases.

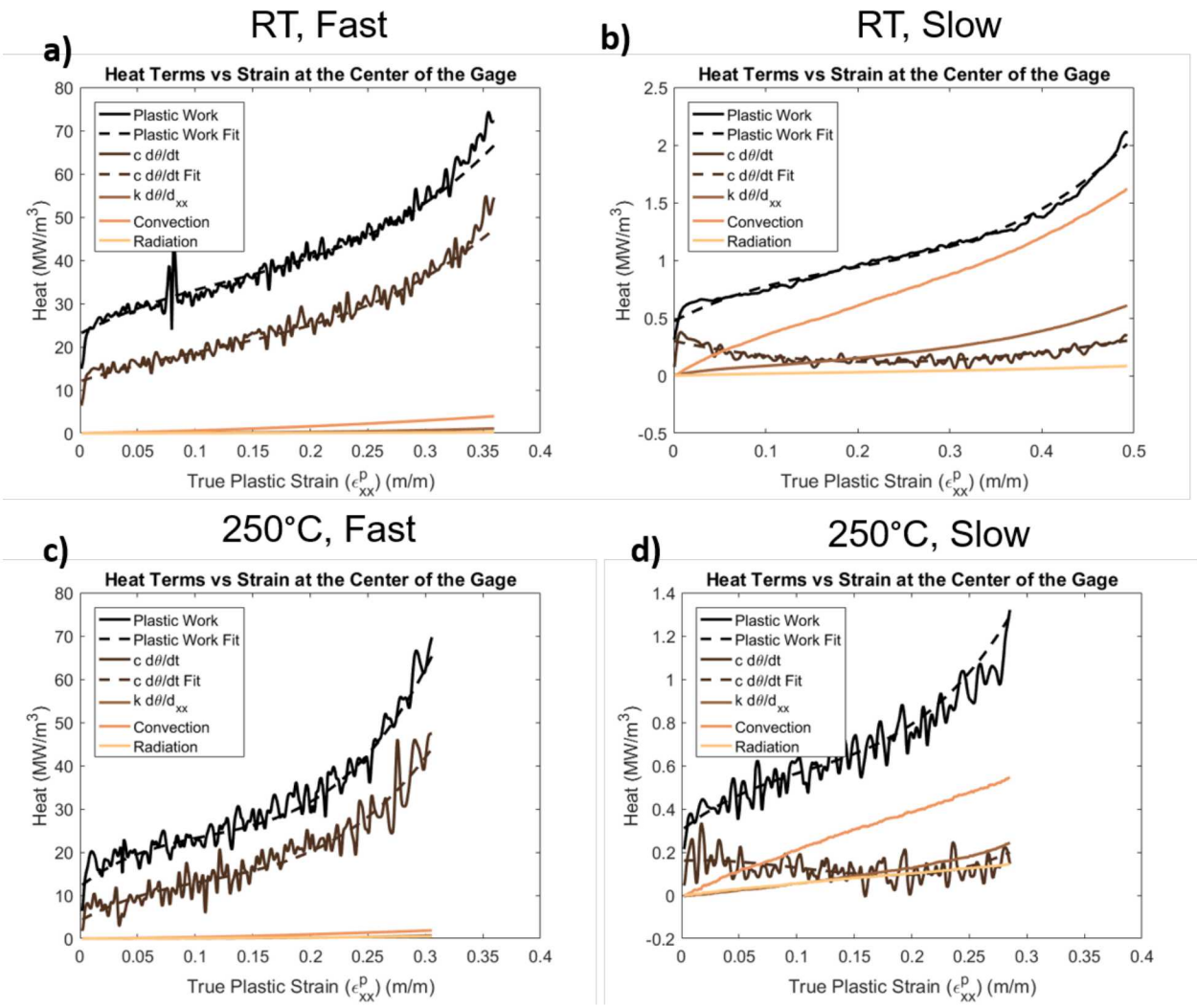

Figure 3.8: Each of the heat flux terms in Equation 3.3 as a funtion of strain rate and soak temperature for (a) Fast, RT, (b) Slow, RT, (c) Fast, 250^{o}C, and (d) Slow, 250^{o}C.

With all of this in mind, as a preliminary method to compile the data, we did attempt a crude fit of the noisier signals, which was then fed into the calculation of β shown in Figure 3.9. For the fast rate (at both temperatures), we have a high degree of confidence in the results and observe the curves are relatively close to one another with the exception of at low plastic strain. This suggests that in the case of conversion of plastic work to heat, the moderate soak temperature differences studied here are dominated by the strain rate effects. This is not directly understood from just looking at the stress-strain curves where the samples pulled at the same rate, but at different temperatures, behaved significantly different. However, the changes in temperature were also significantly different, and thus these results confirm combined thermomechanical data is critical towards the understanding of β.

For the slow rates, we observe a similar lower intial β at low strain for the elevated temperature test. Both curves, then increase as in the fast case. The slow room temperature test calculation

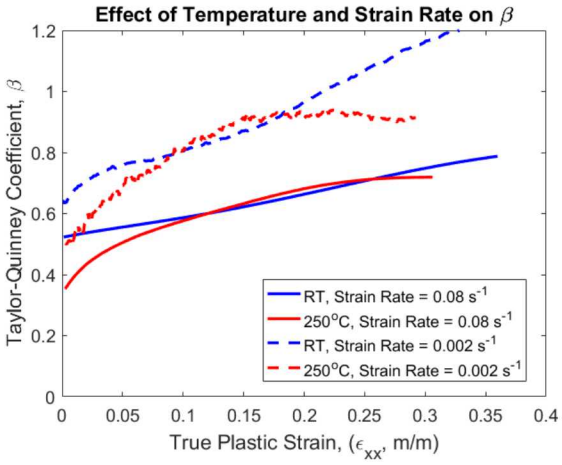

Figure 3.9: β as a function of strain rate and soak temperature using cubic fits for the plastic work rate and c$d\theta$ /dt terms.

yields a value for $\beta > 1$, which is not phyically possible. This author believes the most likely reason for the rapid, non-physical, increase in β is error in the convection measurements, but error could also reside in the plastic work calculation (1-D stress state). Possibilities to correct this error are discussed in future work. As a final note, if the convection measurements are to believed (e.g. at $\varepsilon_{xx} < 0.2$), both slow rates yielded a higher β than the fast rate results. The reason for this difference is a subject of great interest in future work.

Chapter 4

Conclusions and Future Work

4.1 Conclusions

A method to link IR and DIC deformation fields for a uniaxial tensile test in an environmental chamber was developed and the tensile response at two rates (0.002 s^{-1} and 0.08 s^{-1}) and two temperatures (room temperature and 250^{o}C) was characterized. The results were used to calculate the Taylor-Quinney coefficient, β. At the faster (0.08 s^{-1}) rate and room temperature, the method developed was sucessful. The noise in the measurements was small compared to prior literature results, and β was found to vary with plastic strain (and did not equal the often accepted value of 0.9)– a conclusion of importance to thermomechanical modeling efforts. The values for β at the same rate at an elevated temperature similarly varied with plastic strain and followed the same general trend as the room temperature case, with a slightly lower initial β. The slow rate testing proved more difficult due to uncertainties in convection measurements. However, if the results are accurate, β was significantly different at the slow rate when compared to the high rate results.

4.2 Future Work

The technique was validated for fast quasi-static rates, but not for slow rates. The main improvement required is higher accuracy convection measurements. The proposed method(s) to do so are:

- Develop a thermal model of the environmental chamber.
- Limit convection (toggling fan on and off) or remove completely using a vacuum tube.
- Use the IR camera to more accurately determine a far-field temperature field.

As a final note on convection, several samples were tested at room temperature without the fan and can/should be analyzed in future studies. This analysis would allow us to understand better the slow rate, room temperature results. Additionally, a new higher resolution IR camera and a new oven was purchased that will allow for toggling the fan on and off, which should both improve the signal to noise ratios for high temperature testing as well as room temperature, at the slow rate. Once the convection measurements are improved, the difference in β as a function of rate and

temperature can be more fully understood.

Looking towards the future, a desirable end result would include a 2-D analysis of β, which requires a model to evaluate more than a 1-D state of stress. Higher soak temperatures are also of interest, but would require development of speckling techniques that are not paint-based. More broadly, these initial results suggest that strain rate and temperature effects do exist and warrent further studying. Though we calculated β, a microstructural understanding of the results is lacking, which could explain the differences we saw. A variety of experiments are envisioned to observe the mechanisms that are causing these differences– one of the most interesting ones being a series of interrupted tests to separate rate and temperature effects. With a few improvements, we believe this method could be used for a multi-material study, which would include a suite of strain rates (quasi-static to high rate, Kolsy bar) and temperatures, as well as microstructural analysis.

References

[1] Laurence Bodelot, Laurent Sabatier, Eric Charkaluk, and Philippe Dufrnoy. Experimental setup for fully coupled kinematic and thermal measurements at the microstructure scale of an aisi 316l steel. *Materials Science and Engineering A*, 2009.

[2] Sharlotte L.B. Kramer. Characterization of 304l stainless steel laser welds. *SAND2015-9012*, 2015.

[3] P. Rosakis, A.J. Rosakis, G. Ravichandran, and J. Hodowany. A thermodynamic internal variable model for the partition of plastic work into heat and stored energy in metals. *Journal of the Mechanics and Physics of Solids*, 2000.

[4] M.J. Assael and K. Gialou. Measurement of the thermal conductivity of stainless steel aisi 304l up to 550 k. *International Journal of Thermophysics*, 2003.

[5] J. Hodowany, G. Ravichandran, A.J. Rosakis, and P. Rosakis. Partition of plastic work into heat and stored energy in metals. *Experimental Mechanics*, 1999.

[6] Yannis P. Korkolis Paul Knysh. Determination of the fraction of plastic work converted into heat in metals. *Mechanics of Materials*, 2015.

DISTRIBUTION:

1	MS 0557	Thomas Bosiljevac, 01528 (electronic copy)
1	MS 0557	Jhana Gearhart, 01528 (electronic copy)
1	MS 0557	Kimberly Haulenbeek, 01528 (electronic copy)
1	MS 0557	Darrick Jones, 01528 (electronic copy)
1	MS 0557	Sharlotte Kramer, 01528 (electronic copy)
1	MS 0828	Elizabeth Jones, 01512 (electronic copy)
1	MS 0840	Ben Reedlunn, 01554 (electronic copy)
1	MS 0840	Edmundo Corona, 01554 (electronic copy)
1	MS 0840	Eliot Fang, 01554 (electronic copy)
1	MS 0889	Jay Carroll, 01851 (electronic copy)
1	MS 0889	John Laing, 01851 (electronic copy)
1	MS 9042	James Foulk, 08256 (electronic copy)
1	MS 9042	Kyle Karlson, 08259 (electronic copy)
1	MS 0899	Technical Library, 9536 (electronic copy)